


Article

Impact Pressure Distribution Recognition for Large Non-Cooperative Target in Ground Detumbling Experiment

Siqi Peng ¹ , Huibo Zhang ^{2,*}, Chaoqun Qi ¹, Jialiang Xu ^{3,4}, Rui Ma ^{3,4} and Shijie Dai ¹

¹ School of Mechanical Engineering, Hebei University of Technology, Tianjin 300401, China; psq_office@163.com (S.P.); qcq911@163.com (C.Q.); dshj70@163.com (S.D.)

² College of Mechanical and Electrical Engineering, Harbin Engineering University, Harbin 150001, China

³ Tianjin Key Laboratory of Microgravity and Hypogravity Environment Simulation Technology, Tianjin 300301, China; xujialiang024@163.com (J.X.); marui057@163.com (R.M.)

⁴ Tianjin Institute of Aerospace Mechanical and Electrical Equipment, Tianjin 300301, China

* Correspondence: zhanghuibo@hrbeu.edu.cn

Abstract: During the contact between the detumbling end-effector and large non-cooperative target, the recognition of impact pressure distribution is important for estimating the success rate of detumbling mission. To figure out the pressure trends, the ground experiments before the real space mission are necessary. However, due to the drawbacks of the pressure array-like sensor, dynamic characteristics of impact, and unavoidable noise, the accurate dynamic pressure distribution is hard to obtain. In this letter, we propose a recognition method, Impact Pressure Distribution Recognition. The proposed method can quickly generate dynamic impact pressure distribution without limitation on sensor accuracy through pressure data supplement and area correction based on contact model. The analysis results show that our method can efficiently recognize multiple distributed pressure and rebuild the more accurate impact pressure distribution.



Citation: Peng, S.; Zhang, H.; Qi, C.; Xu, J.; Ma, R.; Dai, S. Impact Pressure Distribution Recognition for Large Non-Cooperative Target in Ground Detumbling Experiment. *Aerospace* **2022**, *9*, 226. <https://doi.org/10.3390/aerospace9050226>

Academic Editor: Vladimir S. Aslanov

Received: 14 February 2022

Accepted: 16 April 2022

Published: 20 April 2022

Publisher's Note: MDPI stays neutral with regard to jurisdictional claims in published maps and institutional affiliations.



Copyright: © 2022 by the authors. Licensee MDPI, Basel, Switzerland. This article is an open access article distributed under the terms and conditions of the Creative Commons Attribution (CC BY) license (<https://creativecommons.org/licenses/by/4.0/>).

Keywords: large space debris; detumbling experiment; force sensing; space robotics and automation

1. Introduction

Large non-cooperative target with big quality and volume is mainly derived from the upper stage rocket bodies and expired satellites, and has imposed potential threats on the operational spacecraft in orbit [1–5]. It is impossible for the spacecraft to resist impact damage through self-protection ability. Thus the capturing and removal for large non-cooperative target is of great relevance. Due to the tumbling motion of large non-cooperative target, capturing directly such as net capturing [6], robotic arm [7], and other contact capturing method, is likely to have subsequent consequences like fierce collision and tether wrapping. Conducting a detumbling operation for large non-cooperative target before capturing can attenuate angular momentum to improve the security of capturing mission [8].

Thus, detumbling technologies as the key component of capturing mission, include contact methods and non-contact detumbling methods. Non-contact detumbling methods [9–11], such as thruster plume impingement, electrostatic force, and eddy current, have characteristics of small torque, less impact and long-term operation. Compared to it, contact detumbling methods [12–14] provide larger torque in a shorter term, which include Tethered Space Robot, mechanical impulse and brush contactor. Consequently, studies on the impact reduction method using mechanical impulse with flexible end-effector were developed for the ground detumbling experiment [15], which are aimed at keeping efficiency of detumbling and capturing mission.

To judge the effectiveness of the space detumbling task, it's necessary to calculate the position change of the non-cooperative target. When the flexible end-effector collides with the surface of the non-cooperative target, the impact area and impact pressure distribution

are important parameters for calculating the target position change. However in the real space mission, it is impossible to install sensors on the non-cooperative target. The resultant impact force is the only parameter that can be obtained by the single-axis force sensor mounted between the flexible end and the robot arm. Dynamic impact pressure distribution is impossible to be obtained. Through the ground experiment, we can obtain and understand the characteristics of the distributed forces on the contact surface during the impact. On the basis of accurate impact pressure distribution measurement in this paper, we can carry out the study of the motion of the target due to the impact pressure in the subsequent study. Thus the ground detumbling experiment proposed in Figure 1a is needed for further investigation into the recognition of impact pressure distribution including contact area and distributed force.

To research dynamic impact pressure distribution in the ground experiment, the array-like pressure sensor was used in ground detumbling experiment to collect distributed force data as depicted in Figure 2a. By dividing the responsive area into multiple discrete subelements, array-like pressure sensor can easily provide raw multipoint pressure. However, due to the nonlinearity and hysteresis of pressure sensor and voltage oscillation from fast circuit switching, pressure data heavily relies on sensor characteristics and recognition of dynamic impact performance is difficult. Gaussian distribution and other math model have been used to denoise sensor data [16] in static data processing. And high resolution calibration method based on deep learning can overcome drawbacks of soft pressure sensor [17–20]. Nevertheless, those methods can hardly apply to dynamic distributed pressure data processing for generating dynamic impact pressure distribution.

The goal of this paper is to establish accurate impact pressure distribution including the dynamic impact contact area and the distributed force. Through the pressure data supplement and area correction based on the contact model, the recognition of impact pressure distribution can be achieved. And the recognition result will be a huge help to study the dynamic impact process for the ground detumbling experiment.

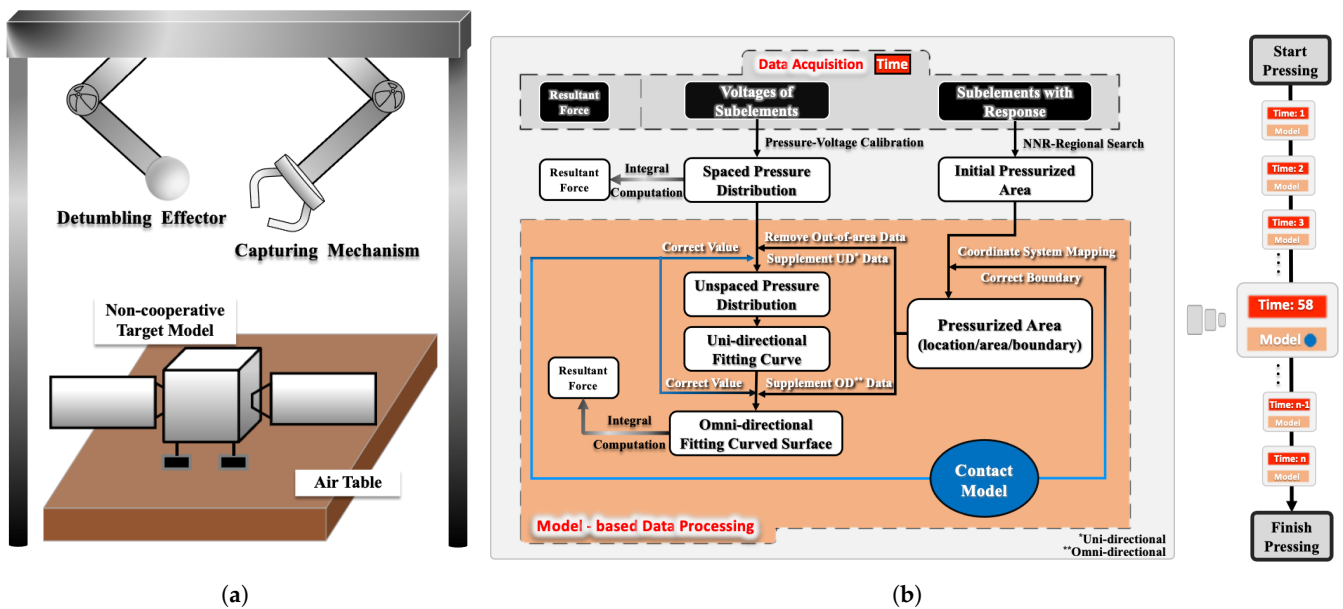


Figure 1. Impact contact experiment and pressure recognition method. (a) Ground detumbling and capturing experiment for large non-cooperative target. (b) Impact Pressure Distribution Recognition (IPDR) method.

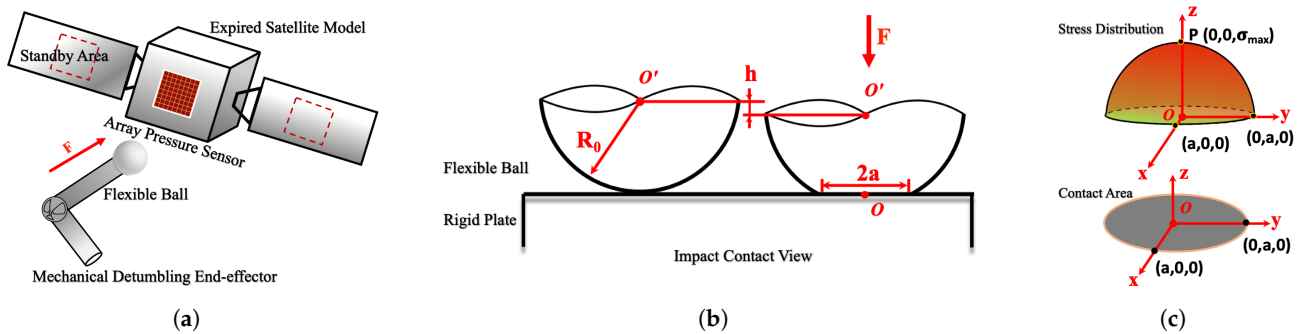


Figure 2. Contact model of mechanical detumbling. (a) Mechanical impulse detumbling mission. (b) Parameters of Hertz contact model. (c) Stress distribution and contact area.

2. Proposed Methods

To recognize contact area and trend of distributed impact pressure, the Impact Pressure Distribution Recognition (IPDR) method mainly process total time-varying data including the value of sensor subelements and responsive sensor areas. The raw data from each sensor subelements is a list of voltage value. And subelements with response consist of the number and location of subelements which have been detected as voltage change. In addition, an interval area without piezoresistive material, which has no capability to detect pressure, exists between any two sensor subelements. Pressure data in interval area should be supplemented.

The IPDR method as illustrated in Figure 1b, is designed for whole pressing process from the start to finish. The Number of Neighboring Response (NNR) is presented to define the response state of neighboring sensor subelements. In each time series (TIME), the IPDR method firstly identifies the center of pressurized area through the region search algorithm based on NNR, in order to obtain initial pressurized area including preliminary area boundary and number of pressurized subelements. And by pressure-voltage calibration, the voltage list of subelements is converted to spaced pressure distribution, which indicates the relative position between impact pressure of each subelement and their pressure values. With the guidance from contact model, the center of initial pressurized area corresponds to the center of theoretical contact area, and meanwhile the boundary is corrected by the theoretical area boundary in order to acquire pressurized area with exact center location and boundary.

In order to preserve the characteristics of the raw data and improve the processing speed, the whole area is divided to multiple strip areas in accordance with the structure of array-like sensor. These strip areas' directions are parallel to each other. The uni-directional data refers to a set of the pressure values of all sensor subelements in one strip area. Meanwhile the omni-directional data consist of all uni-directional data in the whole area. To establish unspaced pressure distribution, the steps of removing data outside the contact area and supplementing uni-directional and omni-directional data for the interval area are taken based on the pressurized area obtained before. And the stress distributed law from contact model is used as a standard to the pressure distribution so that each distributed pressure value can be accurately corrected. After the model-based data processing of IPDR method, the dynamic impact pressure distribution has been supplemented and corrected, and therefore has the capability to accurately describe contact area change and exact pressure distribution in whole impact process. The IPDR method has no limitation of contact model type and array pressure sensor structure so that is well suited to various kinds of impact conditions.

3. Preliminary

3.1. Contact Model

As shown in Figure 2a, the IPDR method can apply to the impact contact process during mechanical detumbling mission. The mechanical detumbling end-effector is equipped with a flexible spherical end, which impacts vertically with a force of F on the surface of expired satellite model. As depicted in Figure 2b, Hertz contact model [21,22] is adopted to describe the impact contact process between a flexible ball with a radius of R_0 and a rigid plate.

As illustrated in Figure 2c, The contact area is a circle with a radius of a , and the maximum stress σ_{max} is located at the center of the circle. According to Hertz formula [23], the maximum stress is expressed as below:

$$\sigma_{max} = \left(\frac{6}{\pi^3} \cdot \frac{1}{R_0^2} \frac{F}{\left(\frac{1-v_1^2}{E_1} + \frac{1-v_2^2}{E_2} \right)^2} \right)^{\frac{1}{3}}, \quad (1)$$

where v_1 and v_2 represent Poisson's ratio of the flexible ball and rigid plate, E_1 and E_2 represent their elastic modulus. The radius of contact area can be calculated as below:

$$a = \left(\frac{3}{4} R_0 \left(\frac{1-v_1^2}{E_1} + \frac{1-v_2^2}{E_2} \right) F \right)^{\frac{1}{3}}. \quad (2)$$

Figure 2c presents the stress distribution of Hertz contact model, and the stress value of each location is computed as below:

$$\sigma(x, y) = \sigma_{max} \left(1 - \frac{x^2 + y^2}{a^2} \right)^{\frac{1}{2}}. \quad (3)$$

When selecting a direction parallel to y-axis, the value of x is fixed in this direction ($x = d$). The stress gradient in this direction can be expressed with the equation below:

$$\sigma'|_{x=d}(y) = \frac{-\sigma_{max} \cdot y}{a^2} \left(1 - \frac{d^2 + y^2}{a^2} \right)^{-\frac{1}{2}}, \quad -a < d < a. \quad (4)$$

Owing to dividing the omni-directional contact area to a certain amount of uni-directional areas, the above formula based on contact model can purposefully apply to IPDR method for distributed pressure data processing.

3.2. Data Acquisition

From the analysis of contact mechanics theory, whether the axial motion of the collided target only affects the trend of the impact pressure distribution over time during the collision. If the target is fixed, the value and impact area of the impact pressure increase gradually with time. If the target is not fixed, the value and impact area of the impact pressure increases and then decreases with time. The experiment in this paper is to verify the accuracy of the impact pressure data collection. So the control variates method is used in the experiment, mainly to study the law of impact pressure distribution generated by the impact of different velocities on fixed target. By doing this, this impact pressure change by different velocities is estimable so that it is better to determine the accuracy of the impact pressure distribution obtained from the proposed method. For this specific research purpose, detumbling end-effector is located above a table surface and is approaching the target object from the direction perpendicular to the table surface. This experimental setup makes it easier to create a stable impact process.

As illustrated in Figure 3a, the experiment setup for impact pressure collection consists of pressurized mechanism, pressure sensor, impact end-effector, and control module. The

flexible silicone ball with the radius of 50 mm is attached to a single-axis force sensor, which can obtain dynamic loading force F as shown in Figure 2b. The single-axis force sensor is a kind of silicon strain sensor. The sensing ranges is -60 N to 60 N and the resolution is $1/200\text{ N}$. And in order to get impact pressure distribution, the array-like pressure sensor is plated on the rigid surface under the impact end-effector. The Poisson’s ratio of the flexible ball and rigid plate are 0.49 and 0.3, and the elastic modulus are 6.1 MPa and 70 GPa. The flexible ball is fixed by screws on the ball seat of the end-effector. It will not be detached due to detumbling torque. In real space detumbling mission, the end-effector is in vertical contact with the target surface, since it’s the most effective and easy to implement operation.

As depicted in Figure 3c,d, the 16×16 pressure matrix sensor with 256 subelements comprises two electrode layers and a middle piezoresistive layer. The overall size is $39\text{ mm} \times 39\text{ mm}$, and each subelement size is $1.5\text{ mm} \times 1.5\text{ mm}$. The spaced area without piezoresistive material exists between any two sensor subelements. The array-like pressure sensor is driven by the signal acquisition and conversion circuit proposed in Figure 3b.

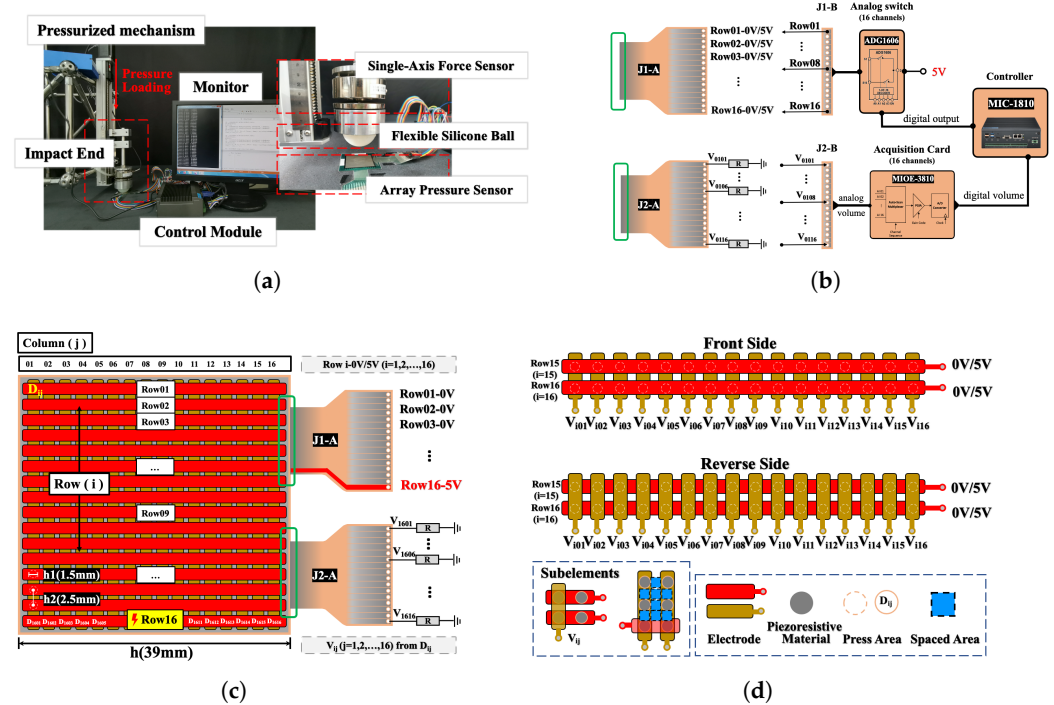


Figure 3. Data acquisition system. (a) Experiment setup for impact pressure collection. (b) Signal acquisition and conversion circuit. (c) Structure of array-like pressure sensor and data reading process. (d) Structure of subelement and area classification.

The circuit sets the high input voltage (5 V) to one row and low input voltage (0 V) to the other rows of the sensor through J1. Due to supplying high input voltage to each row (i) in turn, the control module collects voltage in each column (j) of sensor through J2 to build raw data distribution as follows:

$$V^{TIME} = [V_{i,j}] = \begin{bmatrix} V_{1,j} \\ V_{2,j} \\ \vdots \\ V_{16,j} \end{bmatrix} = \begin{bmatrix} V_{1,1} & V_{1,2} & \cdots & V_{1,16} \\ V_{2,1} & V_{2,2} & \cdots & V_{2,16} \\ \vdots & \vdots & \ddots & \vdots \\ V_{16,1} & V_{16,2} & \cdots & V_{16,16} \end{bmatrix}, \quad (5)$$

where $TIME$ represents a time series of the whole data acquisition process.

4. Experiment Analysis

4.1. Raw Data Distribution

Collected from the ground flexible impact experiment, the raw data format of each time series is a voltage distribution in 256 subelement areas as illustrated in Figure 4. The raw data distribution indicates discrete pressure values and their relative positions, and besides the noise data outside actual contact area.

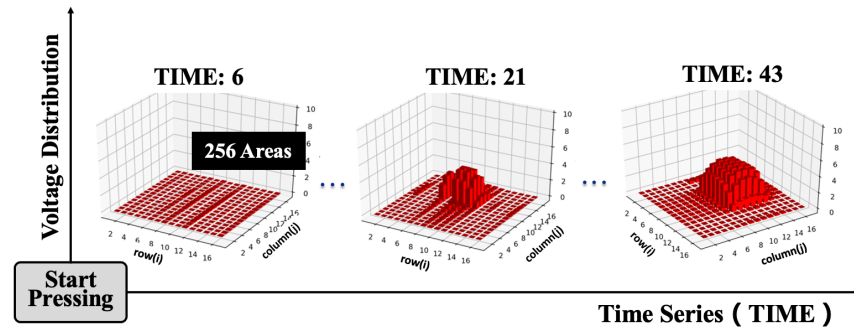


Figure 4. Dynamic raw voltage data distribution.

4.2. Pressurized Area Searching Method

To quickly obtain the pressurized areas from the raw data, we proposed the NNR and NNR-Region Search algorithm. Under the pressing area as shown in Figure 5, the NNR is used to define the response state of neighboring areas around each subelement. The “Response be detected” state represents that this sensor subelement has been captured for a voltage change caused by pressure loading, and a subelement without a voltage change refers to the “No response be detected” state. After calculating NNR and searching the coordinate of maximum pressure, the preliminary data including spaced pressurized areas and contact area center can be realized for the further data processing.

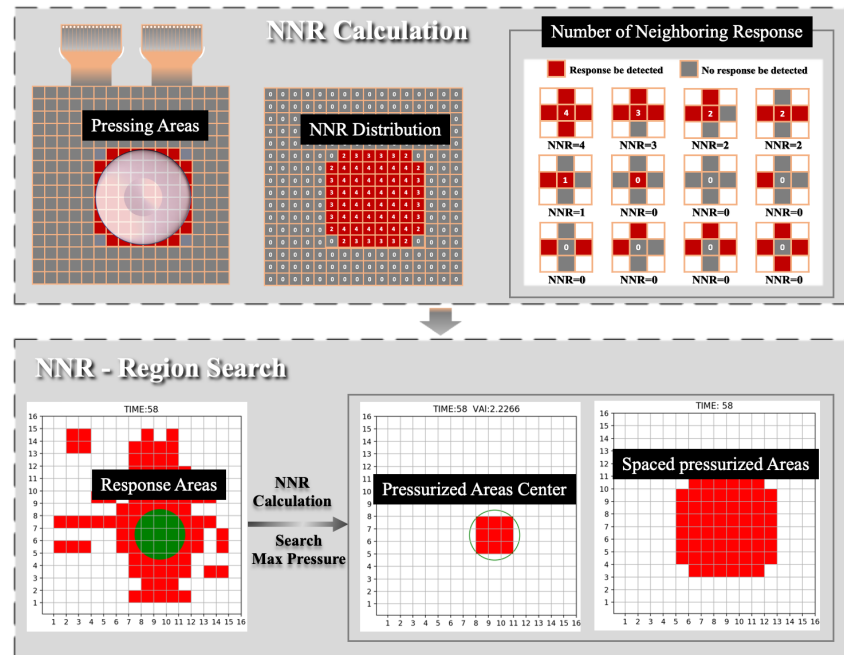


Figure 5. NNR calculation and region search algorithm.

4.3. Impact Pressure Data Processing

According to the IPDR method proposed above and the Hertz formulas, the omnidirectional data has been divided to 16 sets of uni-directional data to improve the data pro-

cessing speed. Focusing on a set of uni-directional data in the 123rd time series (TIME:123) as a random example, the raw format is voltage data collected from 16 columns in the 8th row as illustrated in Figure 6.

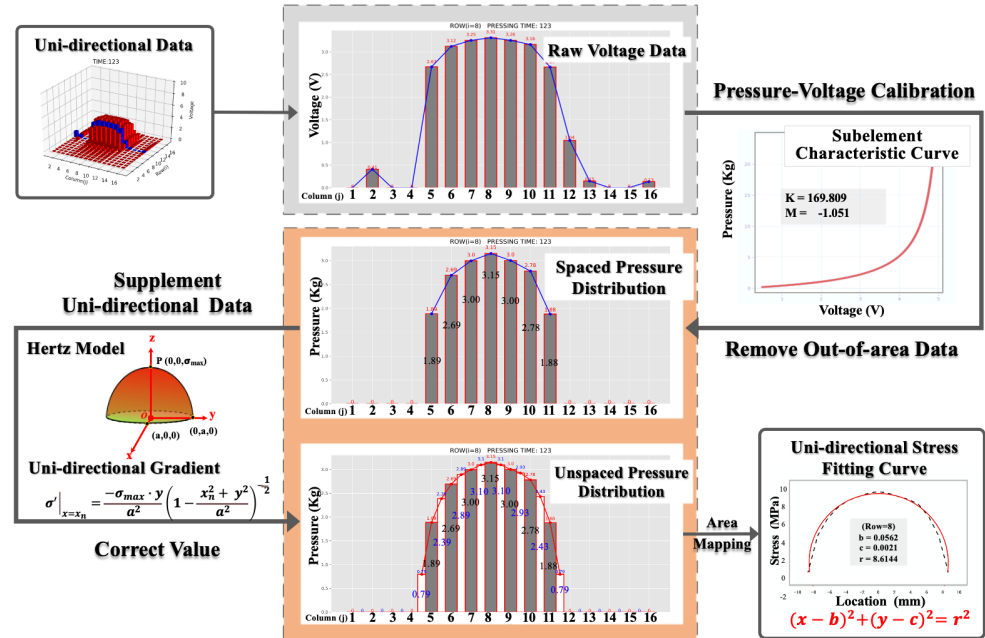


Figure 6. Procedures of uni-directional data processing.

The data pressure distribution of the 8th row in the 123rd time series is expressed as below:

$$V_{i=8}^{123} = [V_{8,j}] = [V_{8,1} \ V_{8,2} \ V_{8,3} \ \dots \ V_{8,15} \ V_{8,16}], \quad j = 1, 2, 3, \dots, 16. \quad (6)$$

The main processing steps consist of pressure-voltage calibration, removing data outside contact area, supplementing uni-directional data, and correcting pressure values. The first step is the conversion from voltage to pressure based on the subelement characteristic curve expressed as below:

$$F_{i,j} = K \cdot (V_{i,j})^M. \quad (7)$$

By the calibration before using the array-like pressure sensor, the values of “K” and “M” can be determined. The values for every sensor subelement are very similar and the most frequent values are shown in Figure 6. After the conversion, the uni-directional pressure distribution in the 8th row has been generated as follow:

$$F_{i=8}^{123} = [F_{8,j}] = [F_{8,1} \ F_{8,2} \ F_{8,3} \ \dots \ F_{8,15} \ F_{8,16}], \quad j = 1, 2, 3, \dots, 16. \quad (8)$$

Based on the stress distribution equation of the particular direction given in Section 3, the pressure value of each interval area between subelements can be calculated and verified by its corresponding location and the two existing neighboring pressure data. The supplementary pressure can be calculated as below:

$$S_{i,j} = \frac{1}{2}(F_{i,j} + F_{i,j+1}) + A(\delta - 1) \cdot \sigma(x, y), \quad j = 1, 2, 3, \dots, 15. \quad (9)$$

The $\sigma(x, y)$ refers to the stress at position (x, y) in the interval area between subelements. The A refers to the area size of an sensor subelement. The δ is a modified coefficient related to the position of the interval area and can be calculated as below:

$$\delta = \frac{1}{2} \left(1 - \frac{F_{i,j} + F_{i,j+1}}{2A \cdot \sigma(x,y)} \right) + 1. \tag{10}$$

The uni-directional unspaced pressure distribution has been supplemented and corrected in order to improve the capability for describing the impact pressure distribution of an impact process.

According to the pressurized area corrected by the Hertz contact model, the pressure data of each subelement can be apparently classified as intra-regional and out-of-area data. The out-of-area data is set to zero. The removal of out-of-area pressure data regarded as noise contributes greatly to the impact pressure distribution. As for the 8th row, the pressure values in these 9 columns ($j = 1, 2, 3, 4, 12, 13, 14, 15, 16$) are out-of-area data, so they are set to zero. The unspaced pressure distribution includes 16 raw values ($F_{i,j}$) and 15 supplementary values ($S_{i,j}$). The final pressure distribution of the 8th row in the 123rd time series after IPDR method is expressed as below:

$$F_{i=8}^{123} = [0 \cdot \cdot \cdot 0 S_{8,4} F_{8,5} S_{8,5} F_{8,6} S_{8,6} F_{8,7} S_{8,7} F_{8,8} S_{8,8} F_{8,9} S_{8,9} F_{8,10} S_{8,10} F_{8,11} S_{8,11} 0 \cdot \cdot \cdot 0]. \tag{11}$$

To verify the superiority of this distribution, we calculate stress value and build uni-directional stress fitting curve. The fitting result shows that the stress distribution satisfies circular function and this circle center is greatly close to the ideal center of contact area. Compared to raw data, the new data after IPDR method has the smaller residual sum of squares (RSS) in the whole impact process as shown in Figure 7a. If the RSS is smaller, it proves that the curve fit is better. After the IPDR method, the new data has a better performance than the original data in terms of the degree of fit. The most prominent aspect of this graph indicates that the coefficient of determination ($R^2 = 0.99956$) in the 123rd time series, which refers to the excellent goodness of fit.

As demonstrated in Figure 8, the omni-directional pressure data processing includes 16 times of uni-directional data processing for total rows, supplementing omni-directional interval data, and correcting pressure values. Through the stress-pressure transformation, the omni-directional stress distribution can be constructed and the fitting curved surface conforms to the hemispherical equation. And the location deviation of stress distribution center, as shown in Figure 7b, represents the variable deviation between the center of the contact area and the center of fitting stress distribution. As the contact area becomes larger, the amount of sensor data increases so that the fit bias gradually decreases and tends to zero.

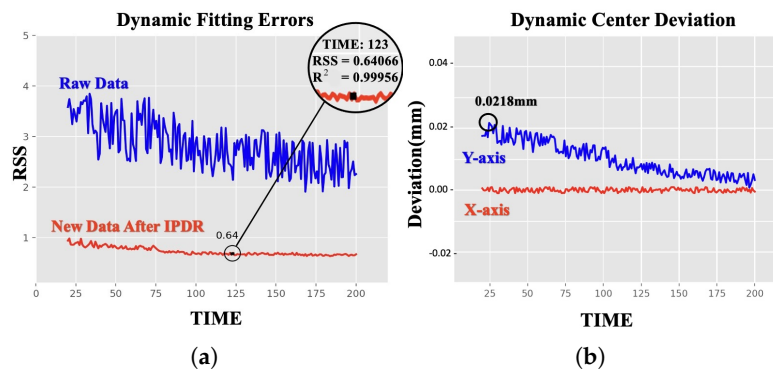


Figure 7. Fitting Error Analysis. (a) Dynamic fitting residual sum of squares for uni-directional data processing. (b) The location deviation of stress distribution center for omni-directional data processing.

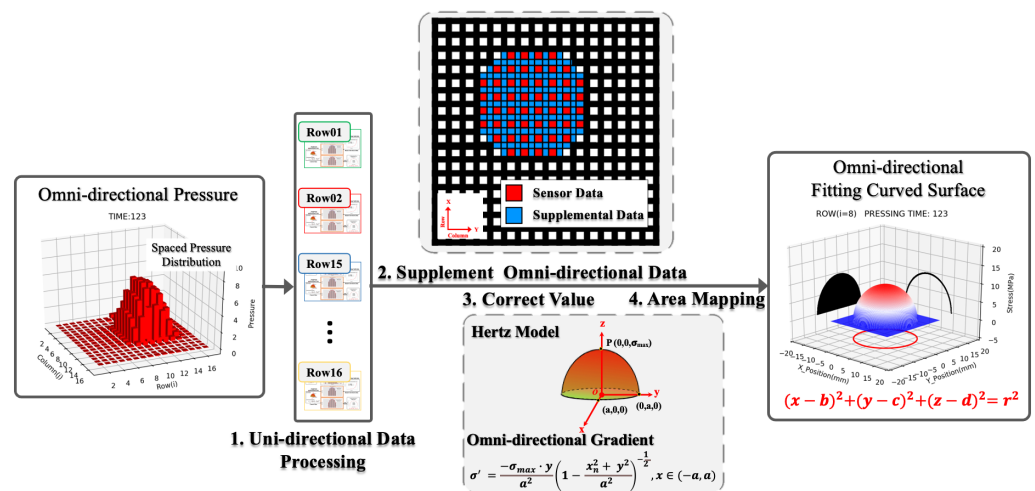


Figure 8. Procedures of omni-directional data processing.

4.4. Effectiveness Analysis of IPDR Method

After above procedures, we generated an accurate impact pressure distribution that reserves the necessary characteristic of raw sensor data and meanwhile has a big improvement in data precision. To study the effectiveness of IPDR method, three resultant forces during complete impact process has been compared as shown in Figure 9.

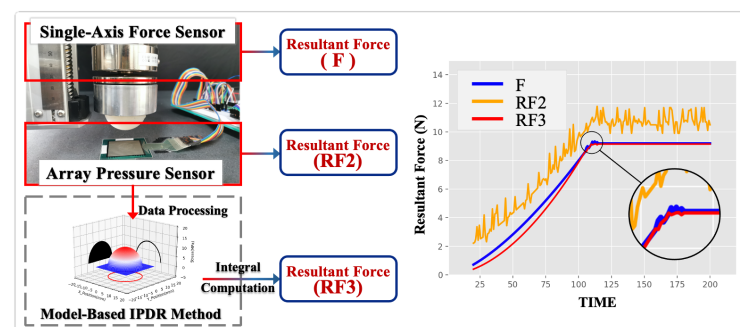


Figure 9. Comparison of resultant forces from data acquisition experiment.

F refers to the dynamic loading force in Equation (1), which is collected directly from the single-axis force sensor in ground impact experiment. The F is an accurate resultant force. By comparing with it, the accuracy of $RF2$ and $RF3$ can be analyzed. $RF2$ is a resultant force calculated by raw discrete data from array-like pressure sensor, and in contrast $RF3$ is a result of the integral computation of the stress distribution generated by IPDR method. During the phase of increasing impact pressure, $RF3$ not only presents the same trend as F but also is gradually approaching the curve of F . Additionally at the turn of F curve, $RF3$ can precisely restore and present the dynamic properties of impact pressure. And $RF3$ also shows a good performance in the late stage with steady pressure. However $RF2$ has an obvious noisy phenomenon and retardation particularly at the turn of F curve. In summary, the IPDR method has been proved efficient to dynamic pressure processing especially in the flexible impact condition with variable pressure and contact area.

5. Conclusions

An impact pressure distribution recognition method called IPDR was proposed in this letter, in order to establish the dynamic impact pressure distribution. The IPDR method mainly includes the pressure data supplement and area correction based on contact model, in order to overcome the drawbacks of the array-like pressure sensor and the difficulty of recognizing dynamic distributed pressure. Through the IPDR method, the accurate contact

area and distributed pressure can be obtained. The impact experiment results show that the IPDR method can achieve dynamic data processing and establish a more accurate impact pressure distribution.

In future work, we would like to build an impact pressure distribution prediction system based on IPDR method for a real space mission. Ground experiments and IPDR method can provide training data for the prediction system. Thus, with the resultant force from the end-effector as the prediction input, we can easily obtain the impact pressure distribution on the target surface.

Author Contributions: Conceptualization, S.P. and H.Z.; methodology, H.Z.; software, S.P.; validation, S.P., H.Z. and C.Q.; writing—original draft preparation, S.P.; writing—review and editing, S.P. and S.D.; supervision, S.D.; funding acquisition, H.Z., J.X. and R.M. All authors have read and agreed to the published version of the manuscript.

Funding: This research was funded by the National Natural Science Foundation of China (Grant No.U21B200193), Tianjin Key Laboratory of Microgravity Environment Simulation Technology Open Subjects (Grant No.WDZL-2021-02), Open Fund Project of Space Intelligent Control Technology Laboratory (Grant No.6142208200101) and Graduate Innovation Grant Program funded by the Education Department of Hebei Province (Grant No.CXZZSS2021031, CXZZSS2021028).

Institutional Review Board Statement: Not applicable.

Informed Consent Statement: Not applicable.

Data Availability Statement: Not applicable.

Conflicts of Interest: The authors declare no conflict of interest.

References

1. Murtaza, A.; Pirzada, S.J.H.; Xu, T.; Liu, J. Orbital debris threat for space sustainability and way forward (Review Article). *IEEE Access* **2020**, *8*, 61000–61019. [[CrossRef](#)]
2. Gao, X.; Liang, B.; Xu, W. Attitude determination of large non-cooperative spacecrafts in final approach. In Proceedings of the 11th International Conference on Control Automation Robotics & Vision, Singapore, 7–10 December 2010.
3. Shan, M.; Guo, J.; Gill, E. Review and comparison of active space debris capturing and removal methods. *Prog. Aerosp. Sci.* **2016**, *80*, 18–32. [[CrossRef](#)]
4. Koryanov, V.V.; Kazakovtsev, V.P.; Toporkov, A.G.; Nedogarak, A.A. Using inflatable structures to remove space debris from orbit. In Proceedings of the IEEE 10th International Conference on Mechanical and Aerospace Engineering, Brussels, Belgium, 22–25 July 2019.
5. Liou, J.C. Engineering and technology challenges for active debris removal. *Prog. Propuls. Phys.* **2013**, *4*, 735–748.
6. Medina, A. Validation results of satellite mock-up capturing experiment using nets. *Acta Astronaut.* **2017**, *134*, 314–332. [[CrossRef](#)]
7. Liu, X.; Zhang, X.; Cai, G.; Wang, M. A collision control strategy for detumbling a non-cooperative spacecraft by a robotic arm. *Multibody Syst. Dyn.* **2021**, *53*, 1–31. [[CrossRef](#)]
8. Sun, K.; Wang, Z.; Zhang, Y.; Liu, H. Detumbling space debris via thruster plume impingement. In Proceedings of the IEEE 3rd Advanced Information Technology, Electronic and Automation Control Conference (IAEAC), Chongqing, China, 12–14 October 2018.
9. Nakajima, Y. Detumbling space debris via thruster plume impingement. In Proceedings of the AIAA/AAS Astrodynamics Specialist Conference, Long Beach, CA, USA, 13–16 September 2016.
10. Bennett, T.; Schaub, H. Touchless electrostatic three-dimensional detumbling of large axi-symmetric debris. *J. Astronaut. Sci.* **2015**, *62*, 233–253. [[CrossRef](#)]
11. Sugai, F.; Abiko, S.; Tsujita, T.; Jiang, X.; Uchiyama, M. Detumbling an uncontrolled satellite with contactless force by using an eddy current brake. In Proceedings of the IEEE Transactions on Aerospace and Electronic Systems, Tokyo, Japan, 3–7 November 2013.
12. Wang, D.; Huang, P.; Meng, Z. Coordinated stabilization of tumbling targets using tethered space manipulators. *IEEE Trans. Aerosp. Electron. Syst.* **2015**, *51*, 2420–2432. [[CrossRef](#)]
13. Amel'kin, N.I.; Kholoshchak, V.V. Rotational motion of a non-symmetrical satellite with a damper in a circular orbit. *Mech. Solids* **2019**, *83*, 190–203. [[CrossRef](#)]
14. Nishida, S.I.; Kawamoto, S. Strategy for capturing of a tumbling space debris. *Acta Astronaut.* **2011**, *68*, 113–120. [[CrossRef](#)]
15. Kawamoto, S.; Matsumoto, K.; Wakabayashi, S. Ground Experiment of Mechanical Impulse Method for Uncontrollable Satellite Capturing. In Proceedings of the 6th International Symposium on Artificial Intelligence and Robotics & Automation in Space: i-SAIRAS 2001, Montreal, QC, Canada, 18–22 June 2001.

16. Khademi, W.; Rao, S.; Minnerath, C.; Hagen, G.; Ventura, J. Self-Supervised Poisson-Gaussian Denoising. In Proceedings of the IEEE Winter Conference on Applications of Computer Vision, Waikoloa, HI, USA, 3–8 January 2021.
17. Kim, M.; Choi, H.; Cho, K.J.; Jo, S. Single to Multi: Data-Driven High Resolution Calibration Method for Piezoresistive Sensor Array. *IEEE Robot. Autom. Lett.* **2021**, *6*, 4970–4977. [[CrossRef](#)]
18. Han, S.; Kim, T.; Kim, D.; Park, Y.-L.; Jo, S. Use of deep learning for characterization of microfluidic soft sensors. *IEEE Robot. Autom. Lett.* **2018**, *3*, 873–880. [[CrossRef](#)]
19. Valle-Lopera, D.A.; Castaño-Franco, A.F.; Gallego-Londoño, J.; Hernández-Valdivieso, A.M. Test and fabrication of piezoresistive sensors for contact pressure measurement. *Rev. Fac. Ing.* **2017**, *82*, 47–52. [[CrossRef](#)]
20. Wang, L.; Nan, M.; Lei, M.; Ling, Y.; Lv, D. Space resolution improvement for pressure measurement by using a single conductive polymer composite sheet in area array. *Sens. Actuators A Phys.* **2019**, *295*, 324–335. [[CrossRef](#)]
21. Jin, D.; Hu, H.; Wu, Z. Analysis of Vibro-Impacting Flexible Beams Based on Hertzian Contact Model. *J. Vib. Eng.* **1998**, *11*, 46–51.
22. Alluhydan, K.; Razzaghi, P.; Hurmuzlu, Y. On planar impacts of cylinders and balls. *J. Appl. Mech.* **2019**, *86*, 071009. [[CrossRef](#)]
23. Johnson, K.L. *Contact Mechanics*, 3rd ed.; Cambridge University Press: Cambridge, UK, 1985.